One-Step Hydrothermal Synthesis of Precious Metal-Doped Titanium Dioxide−Graphene Oxide Composites for Photocatalytic Conversion of CO$_2$ to Ethanol

Napat Lertthanaphol, Natpichan Pienutsa, Kittapas Chusri, Thirawit Sornsuchat, Prowpatchara Chanthara, Panpailin Seeharaj, Pattaraporn Kim-Lohsoontorn, and Sira Srinives*

Read Online

ACCESS | Metrics & More | Article Recommendations | Supporting Information

ABSTRACT: We utilized a one-step hydrothermal process for the synthesis of precious metal-doped titanium dioxide (TiO$_2$)/ graphene oxide (GO) composites. The metal-doped TiO$_2$/GO composites, including silver−TiO$_2$/GO (Ag−TiO$_2$/GO), palladium−TiO$_2$/GO (Pd−TiO$_2$/GO), and copper−TiO$_2$/GO (Cu− TiO$_2$/GO), were synthesized by mixing a metal precursor, titanium butoxide, and graphene oxide in a water−ethanol mixture in an autoclave hydrothermal reactor. The photocatalytic performance of the composites was tested in the photoreduction of carbon dioxide (CO$_2$) to ethanol. Ag−TiO$_2$/GO, Pd−TiO$_2$/GO, and Cu−TiO$_2$/ GO exhibited an ethanol production rate of 109, 125, and 233 μmol/g$_{cat}$ h, respectively. The outstanding performances of Cu− TiO$_2$/GO can be attributed to a combined effect of key parameters, including optical band gap, crystallite size, and BET surface area.
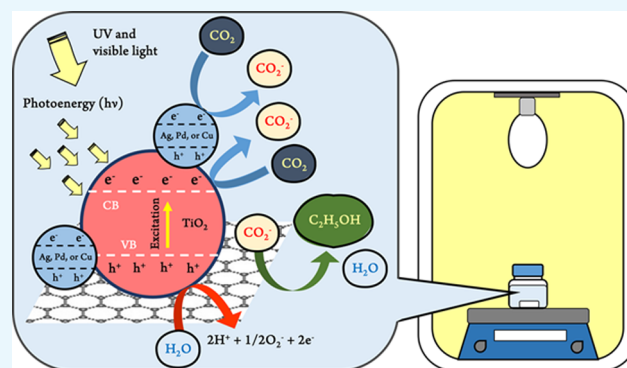
INTRODUCTION

Carbon capture, utilization, and storage (CCUS) is a research and industrial approach for managing CO$_2$. CO$_2$ is either captured, converted to high-value products, or stored underground. Researchers worldwide have contributed to the continual improvement of CCUS technologies, but there are several issues to tackle.[1]

Photoreduction of CO$_2$ to liquid fuels is a potential approach to CO$_2$ conversion to high-value products. It involves the coupling of photoelectrons, generated by a photocatalyst, and dissolving CO$_2$ in an aqueous medium. This triggers the catalytic transformation of CO$_2$ into liquid fuels, such as methanol and ethanol.[2,3] The major key to the approach is assistance from a good photocatalyst, such as zinc oxide (ZnO) or titanium dioxide (TiO$_2$).[4] The photocatalyst utilizes photon energy from light, mainly in the ultraviolet region (UV), to generate photoelectrons that assist in the photoreaction. TiO$_2$ is particularly well known for its performance in water purification.[5,6] It is commercially available, chemically stable, and relatively nontoxic. However, the role of TiO$_2$ is limited by its large energy band gap (3.2– 3.5 eV), narrow light adsorption range, and fast electron−hole recombination rates,[3,7] which lead to a slow photoreaction and inadequate production yield. Precious metals, such as silver (Ag), palladium (Pd), and copper (Cu),[8] have been shown to enhance the photoactivity of TiO$_2$ by providing a transition state for photoelectrons to separate from holes and interact

with other active radicals.[9] Such acts decrease the band gap energy and reduce the electron−hole recombination rate, leading to more photoelectrons becoming involved in the photoreaction and better photoactivity of the photocatalyst. In another approach, immobilization of TiO$_2$ on carbon nanostructures, such as carbon nanotubes and graphene,[10−13] was found to extend the light adsorption range from UV to the visible region. It can also create interfaces between TiO$_2$ and carbon nanostructures that serve as N−P heterojunctions. The heterojunctions enhance separation between photoinduced electrons and holes, promoting photoactivity of such materials.[14]

Graphene is a 2D carbon nanostructure with outstanding charge transfer abilities, chemical stability, and optical properties.[12,15,16] It can be chemically synthesized using a chemical exfoliation approach to yield graphene oxide (GO). This provides a multilayered graphene sheet with functional groups, such as carboxyl, hydroxyl, and epoxy. Interactions between the functional groups and metal precursors lead to the
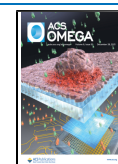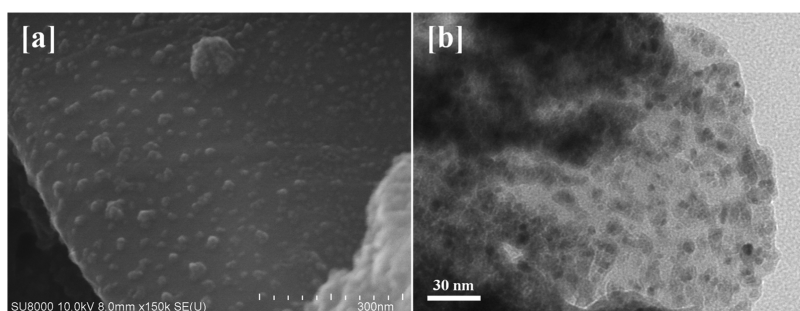
Figure 1. SEM image (a) and TEM image (b) of the TiO$_2$/GO composite, showing distribution of TiO$_2$ nanoparticles on the GO sheet.
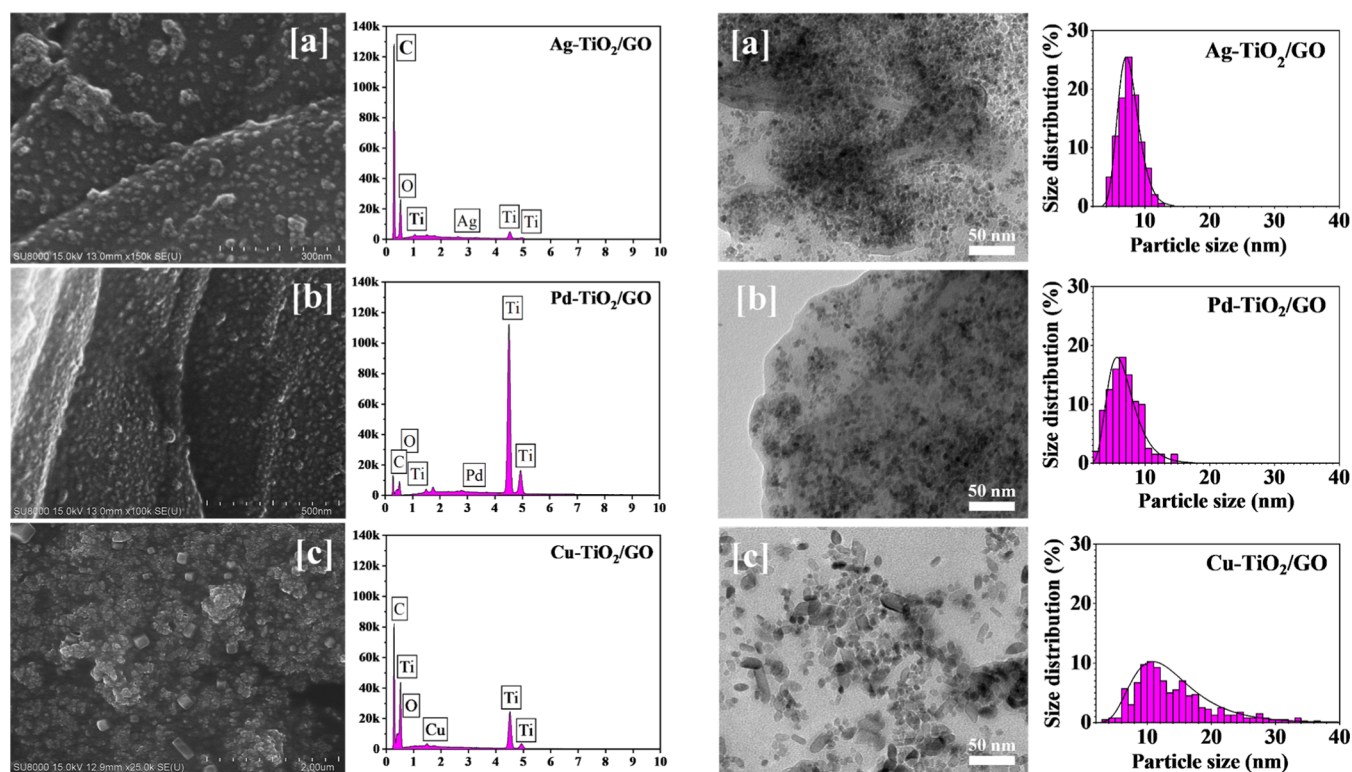

Figure 2. SEM images with EDS spectra (LEFT) and TEM images with particle size distribution (RIGHT) for (a) Ag−TiO$_2$/GO, (b) Pd−TiO$_2$/GO, and (c) Cu−TiO$_2$/GO composites.

accumulation of metal ions and eventually immobilization of metal nanoparticles on the GO sheet.[11] The TiO$_2$/graphene composite is a high-performance photocatalyst with enhanced light adsorption and high surface activity. Various methods have been demonstrated for the synthesis of TiO$_2$/graphene composites, including the sol−gel,[17,18] solvothermal,[19−21] and hydrothermal methods.[22−25] The hydrothermal method offers good control over the growth of TiO$_2$ crystal structures and can be carried out at a relatively lower temperature. Because GO can be thermally damaged at a temperature higher than 150 °C,[26,27] the lower synthesis temperature can be of great advantage. Khalid and his team[28] synthesized Cu−TiO$_2$ nanoparticles using the sol−gel technique and composited Cu−TiO$_2$ with graphene using a hydrothermal process. The composites exhibited a wide range of light absorption covering UV and visible light regions and provided better photoactivity than the Cu−TiO$_2$ particles and TiO$_2$/graphene. Song and his team[29] synthesized a Pd−TiO$_2$/graphene composite by incorporating TiO$_2$ nanoballs on graphene using a poly (diallyl dimethyl ammonium chloride) linker. The composite was

introduced to the palladium chloride along with ammonia solution and heated in a hydrothermal reactor. Katsarakis[9] mixed P25 TiO$_2$ with a silver nitrate precursor along with a dimethylamine borane reducing agent to obtain an Ag−TiO$_2$ powder. The powder was dispersed in a water−ethanol mixture and introduced to GO in a hydrothermal reactor. The Ag−TiO$_2$/GO composite showed outstanding photoactivity in decoloring methylene blue.

In this work, we synthesized Ag−TiO$_2$/GO, Pd−TiO$_2$/GO, and Cu−TiO$_2$/GO composites using a one-step hydrothermal method. The method yielded high-quality composites with metal nanoparticles distributed on GO sheets. The composites were utilized in the photoreduction of CO$_2$ to ethanol and were characterized for optical, geometrical, chemical, and crystallographic properties. Analytical instruments, including a UV−visible spectrophotometer, a scanning electron micro-scope (SEM), a transmission electron microscope (TEM), an energy dispersive X-ray spectrometer (EDS), an X-ray photoelectron spectrometer (XPS), a Fourier transform infrared spectrometer (FTIR), a thermogravimetric analyzer

(TGA), an Autosorb surface analyzer for conducting Brunauer−Emmett−Teller (BET) and Barrett−Joyner−Halenda (BJH) surface area measurements, an X-ray fluorescence spectrometer (XRF), and an X-ray diffractometer (XRD) were used.

■ RESULTS AND DISCUSSION

Sample Characterizations. The TiO_2/GO composite, as observed using the scanning electron microscope (Figure 1a) and transmission electron microscope (Figure 1b), contains TiO_2 nanoparticles, distributed at an average size of ∼7.7 ± 2.2 nm on the GO sheet. The physical morphology of the Ag−TiO_2/GO, Pd−TiO_2/GO, and Cu−TiO_2/GO composites was also observed using the scanning electron microscope [Figure 2 (LEFT)] and transmission electron microscope [Figure 2 (RIGHT)]. For the Ag−TiO_2/GO composite (Figure 2a), the Ag−TiO_2 nanoparticles were distributed on the GO sheet while Ag and TiO_2 were indistinguishable from one another. The size distribution of the nanoparticle lies between 4 and 12 nm with an average size of 7.6 ± 1.6 nm. The EDS spectra reveal the atomic composition of the Ag−TiO_2 sample, showing the presence of titanium (Ti), oxygen (O), and silver (Ag). For the Pd−TiO_2/GO composite (Figure 2b), the Pd−TiO_2 nanoparticles show a size distribution between 2 and 15 nm with an average diameter of 6.8 ± 2.3 nm. Atomic compositions of Pd, Ti, and O were analyzed by EDS. The size and shape of Ag−TiO_2 and Pd−TiO_2 are of the same scale, while the physical appearance observed from the SEM and TEM particles is close to one another. For Cu−TiO_2/GO (Figure 2c), some of the Cu and TiO_2 nanoparticles on graphene appear to be different, showing a cubic structure of Cu and a round shape of TiO_2 nanoparticles. The particle size distribution of Cu−TiO_2 is relatively broad (7−20 nm) compared to that of the Ag−TiO_2 and Pd−TiO_2. An average diameter of 14.0 ± 6.1 nm was calculated for the Cu−TiO_2 nanoparticles.

The FTIR spectra (Figure 3) reveal chemical functionality on GO and TiO_2/GO, Ag−TiO_2/GO, Pd−TiO_2/GO, and
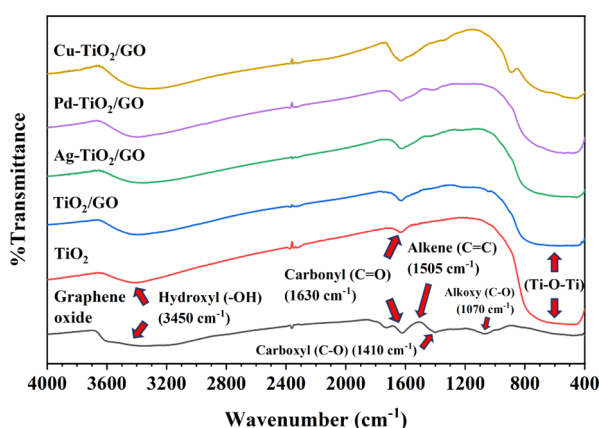
Figure 3. FTIR spectra of GO, TiO_2, Ag−TiO_2/GO, Pd−TiO_2/GO, and Cu−TiO_2/GO.

Cu−TiO_2/GO composites. For GO, IR transmittance peaks appear at 1070, 1410, 1505, 1630, and 3450 cm^{-1}, corresponding to chemical functionalities of alkoxy (C−O), carboxyl (COOH), alkene (C=C), and hydroxyl (C−OH).[30] For TiO_2, a broad peak from 500 to 800 cm^{-1} can be interpreted as Ti−O−Ti vibrations,[27] while the peaks at 3450

and 1630 cm^{-1} are related to hydroxyl and carbonyl groups, respectively. The TiO_2/GO IR transmittance peaks at 1080, 1410, 1530, and 3410 cm^{-1} indicate the presence of alkoxy (C−O), alkene (C=C), carboxyl (COOH), and hydroxyl (C−OH) groups, respectively.[31] The peak at 600 cm^{-1} is related to a combined signal from Ti−O−Ti and Ti−O−C. Peak intensity of the carboxyl, carbonyl, and alkoxy groups is significantly lower in the TiO_2/GO composite, as compared to that of GO. This was found to be because of the functional groups being partially removed from GO during the hydrothermal process.[32] All the precious metal-TiO_2/GO composites, including Ag−TiO_2/GO, Pd−TiO_2/GO, and Cu−TiO_2/GO, show IR transmittance peaks of alkoxy, carboxyl, alkene, carbonyl, and hydroxyl at 1080, 1410, 1530, 1630, and 3410 cm^{-1}. A combined transmittance peak from Ti−O−Ti and Ti−O−C at 600 cm^{-1} can also be observed. No peaks from Ag−Ti, Pd−Ti, and Cu−Ti were observed in our experiment.

The optical properties of GO, TiO_2, TiO_2/GO, and precious metal-TiO_2/GO composites were investigated using UV−vis spectroscopy. A solid suspension was prepared in DI water and transferred to a quartz cuvette. Figure 4 shows the UV−vis
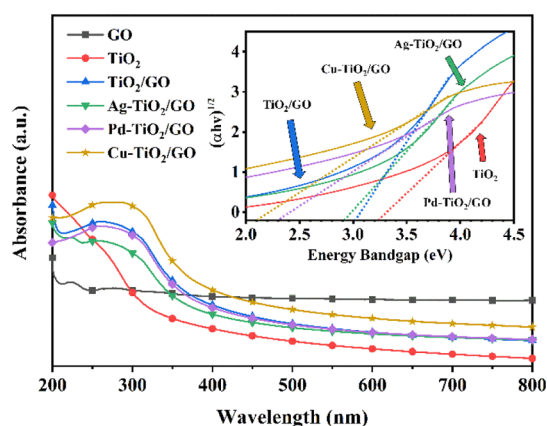
Figure 4. UV−vis spectra of GO, TiO_2, TiO_2/GO, Ag−TiO_2/GO, Pd−TiO_2/GO, and Cu−TiO_2/GO; inset: Tauc plots showing band gap energies of TiO_2, TiO_2/GO, Ag−TiO_2/GO, Pd−TiO_2/GO, and Cu−TiO_2/GO.

spectra of the suspensions, while the Figure 4 inset presents the Tauc plots (eq 13).[30] For GO, the powder displays a broad region of light absorption, ranging from the UV to visible region (200−800 nm), while TiO_2 only absorbs parts of the UV light (200−300 nm).[33,34] For TiO_2/GO, the composite exhibits light absorption in part of the UV and visible regions, revealing superior optical properties for both the TiO_2 and GO.[19,23] The addition of precious metals on the TiO_2/GO composite enhances the optical properties even further. The Cu−TiO_2/GO composite shows superior light absorption ability over Pd−TiO_2/GO and Ag−TiO_2/GO, showing strong light absorption in the UVB and UVC ranges while absorbing light in the visible range. The same trend of light absorption was noticed in the band gap energy of the suspensions [Figure 4 (inset)]. For TiO_2, an optical band gap energy of 3.20 eV was determined and is in good agreement with reported values in the literature.[33,34] For the TiO_2/GO composite, a significant decrease in band gap energy was observed as the energy value decreased to 2.0 eV. The reduction in band gap energy here can be attributed to synergic effects between TiO_2 and GO that promote the generation of photoelectrons and reduce the

pairing rate of electrons and holes.[11,35,36] For Ag−TiO$_2$/GO, Pd−TiO$_2$/GO, and Cu−TiO$_2$/GO, band gap energies of 2.92, 3.09, and 2.11 eV were determined. The composite with precious metals provides slightly higher band gap values compared to that of TiO$_2$/GO. We believe that the coverage of precious metal nanoparticles on TiO$_2$ reduces light exposure of the composite, limiting the number of generated photo-electrons and increasing band gap energy. The Cu−TiO$_2$/GO composite offers the lowest band gap energy among the three, which can be attributed to good adhesion between Cu and TiO$_2$ that yields charge transfer between the two metals.[37]

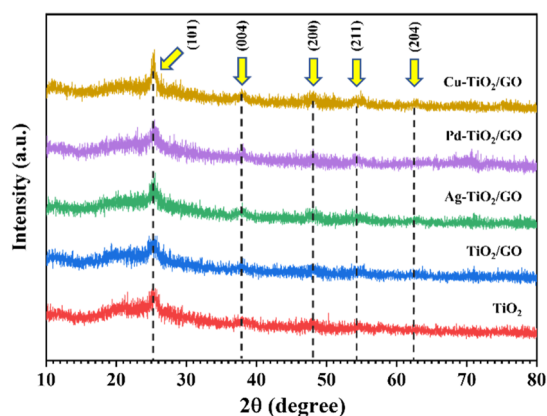The crystallographic structures of GO, TiO$_2$, and composites were analyzed using XRD. Figure 5 reveals the

Figure 5. XRD spectra of TiO$_2$, TiO$_2$/GO, Ag−TiO$_2$/GO, Pd−TiO$_2$/GO, and Cu−TiO$_2$/GO.

XRD spectra of TiO$_2$, TiO$_2$/GO, Ag−TiO$_2$/GO, Pd−TiO$_2$/GO, and Cu−TiO$_2$/GO. For TiO$_2$, the peaks at 25, 38, 48, 54, and 63° (2θ) are related to the (101), (004), (200), (211), and (204) planes of the TiO$_2$ anatase. For the TiO$_2$/GO composite, the XRD spectra also reveal the presence of the TiO$_2$ anatase with no significant signal from the (001) plane of GO (2θ = 12°). For Ag−TiO$_2$/GO, Pd−TiO$_2$/GO, and Cu−TiO$_2$/GO, the composites show XRD peaks at 25, 38, 48, 54,

and 63° (2θ), which can be attributed to the TiO$_2$ anatase structures with no significant signals from Ag,[9] Pd,[29] or Cu.[28] The TiO$_2$ anatase yields an active surface area for the photocatalytic reaction, which results in better photoactivity compared to those of the rutile and brookite TiO$_2$.[38] The active surface of TiO$_2$ also serves as the CO$_2$ adsorption sites, leading to good photoreduction of CO$_2$.[39]

Crystallite sizes of TiO$_2$ and composite samples were calculated using the Debye−Scherrer equation (eq 14), for which the full width at half-maximum (FWHM) of the major peak and diffraction angle (Figure 5) were obtained from the XRD spectra. The crystallite sizes of TiO$_2$, TiO$_2$/GO, Ag−TiO$_2$/GO, and Cu−TiO$_2$/GO were calculated to be 6.6, 7.7, 8.1, 8.1, and 13.1 nm, respectively. Cu−TiO$_2$/GO offers significantly higher crystallite size values, indicating better crystal structures than those of the TiO$_2$ and the other composites.

The chemical composition of the composites was analyzed using XPS (Figure 6). The wide scanning of TiO$_2$/GO composite reveals characteristic peaks of O 1s, Ti 2p, and C 1s, corresponding to binding energies of 530, 458, and 285 eV, respectively (Figure 6a). A C 1s narrow scan of the TiO$_2$/GO composite (Figure 6b) indicates the presence of O−C=O, C=O, and C−C/C=C/C−H, which appear at the binding energies of 288.5, 285.3, and 284.3 eV. The peak at 282.7 eV indicates interactions between TiO$_2$ and GO through the C−Ti bond.[40,41] In another O 1s narrow scan of TiO$_2$/GO (Figure 6c), oxygen-related groups, including C−O, H−O−C/C=O, and Ti−O−Ti are observed at binding energies of 531.4, 529.6, and 528.2 eV, respectively. Another Ti 2p narrow scan of TiO$_2$/GO (Figure 6d) exhibits peaks at 464.3 and 458.5 eV, which can be attributed to Ti 2p$_{1/2}$ and Ti 2p$_{3/2}$. Such peaks can be related to the Ti^{4+} group of the bulk-phase TiO$_2$.[42] The precious metal−TiO$_2$/GO composites were also analyzed using XPS (Figure 7). For Ag−TiO$_2$/GO (Figure 7a), a wide scan reveals binding energies at 532.3, 458.6, 368.2, and 284.8 eV, corresponding to O 1s, Ti 2p, Ag 3d, and C 1s components. A C 1s narrow scan (Figure 7b) shows binding energy peaks at 288.5, 286.4, 284.6, and 282.6 eV that can be
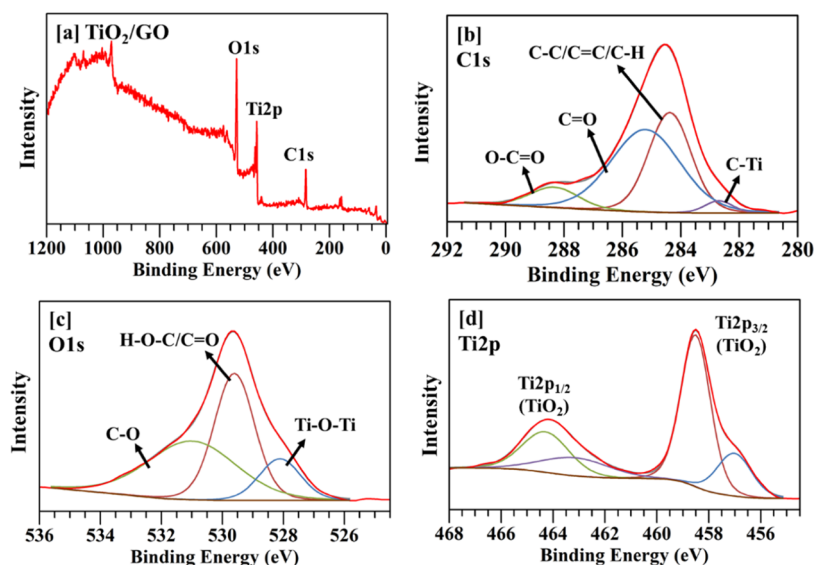
Figure 6. XPS spectra of (a) wide scan of TiO$_2$/GO, (b) narrow scan of C 1s of TiO$_2$/GO, (c) narrow scan of O 1s of TiO$_2$/GO, and (d) narrow scan of Ti 2p of TiO$_2$/GO.
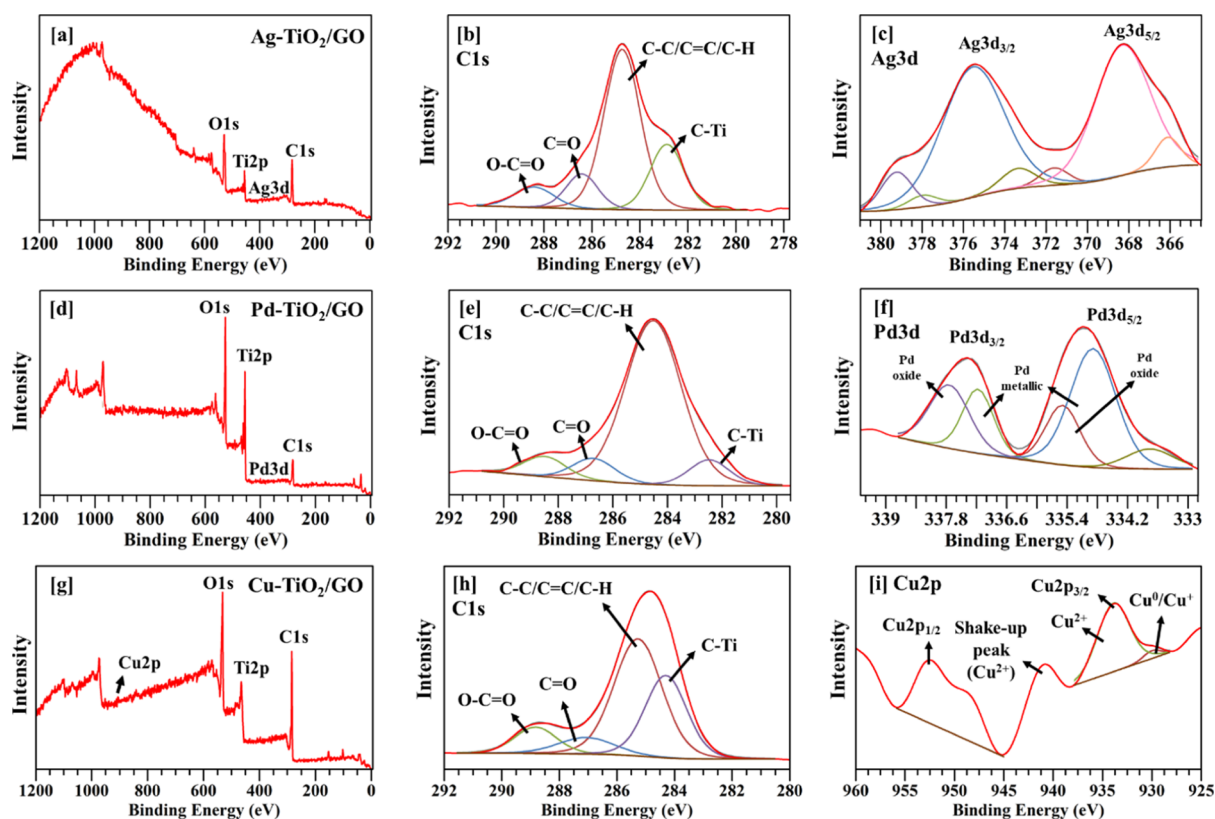
Figure 7. XPS spectra of (a) a wide scan of Ag−TiO$_2$/GO, (b) a narrow scan of C 1s of Ag−TiO$_2$/GO, (c) a narrow scan of Ag 3d of Ag−TiO$_2$/GO, (d) a wide scan of Pd−TiO$_2$/GO, (e) a narrow scan of C 1s of Pd−TiO$_2$/GO, (f) a narrow scan of Pd 3d of Pd−TiO$_2$/GO, (g) a wide scan of Cu−TiO$_2$/GO, (h) a narrow scan of C 1s of Cu−TiO$_2$/GO, and (i) a narrow scan of Cu 2p of Cu−TiO$_2$/GO.

attributed to O−C=O, C=O, C−C/C=C/C−H, and C−Ti groups, respectively. The silver bands were specified in the narrow scan of Ag−TiO$_2$/GO (Figure 7c). The peaks at 375.2 and 368.0 eV correspond to Ag $3d_{3/2}$ and Ag $3d_{1/2}$ and represent the metallic state (Ag^0) of the silver nanoparticles.[43,44] For the Pd−TiO$_2$/GO composite, a wide scan (Figure 7d) shows the presence of the O 1s (526.3 eV), Ti 2p (456.3 eV), Pd 3d (335.1 eV), and C 1s (284.5 eV) peaks.

A C 1s narrow scan of the of Pd−TiO$_2$/GO (Figure 7e) exhibits peaks, which are designated as O−C=O (288.7 eV), C=O (286.8 eV), C−C/C=C/C−H (284.5 eV), and C−Ti (282.5 eV), respectively. The Pd 3d band of Pd−TiO$_2$/GO was studied via a narrow scan to indicate the Pd $3d_{3/2}$ (337.4 eV) and Pd $3d_{1/2}$ (335.1 eV).[45] Oxidative states of Pd were determined by analyzing four subpeaks in the main peaks (Figure 7f),[46] in which the local bands at 337.2 and 334.9 eV can be attributed to metallic Pd and the bands at 337.9 and 335.5 eV were of palladium oxides. Figure 7g shows a wide scan of the Cu−TiO$_2$/GO composite, locating binding energy bands for Cu 2p, O 1s, Ti 2p, and C 1s at 933.1, 531.8, 457.7, and 284.8 eV, respectively. A C 1s narrow scan (Figure 7h) reveals the presence of O−C=O (288.8 eV), C=O (287.2 eV), C−C/C=C/C=H (285.3 eV), and C−Ti (284.3 eV). The Cu 2p band peaks at 952.5 and 933.7 eV (Figure 7i) are attributed to Cu $2p_{1/2}$ and Cu $2p_{3/2}$.[47] The peaks are interpreted as Cu^{2+} of the CuO form.[28] A trace amount of Cu^{1+} and/or Cu^0 was spotted at 933.7 eV, while the shake-up peak of Cu^{2+} appeared at 940 eV.[48]

The BET surface area and pore size of the composite were analyzed using the autosorb surface analyzer. The composites were degassed inside a vacuum chamber and characterized using nitrogen sorption isotherm analysis (Table 1). For TiO$_2$, the BET surface area is 9.82 m^2/g and the pore size is 3.87 nm.

Table 1. Key Parameters of the GO, TiO$_2$, TiO$_2$/GO, Ag−TiO$_2$/GO, Pd−TiO$_2$/GO, and Cu−TiO$_2$/GO Samples

photocatalyst	BET surface area (m^2/g)	band gap energy (eV)	crystallite size (nm)	ethanol production rate (μmol/g$_{cat}$ h)
TiO$_2$	9.82	3.25	6.55	30.63
TiO$_2$/GO	145.77	3.02	7.74	59.10
Ag−TiO$_2$/GO	100.36	2.92	8.11	108.88
Pd−TiO$_2$/GO	214.51	3.09	8.11	124.96
Cu−TiO$_2$/GO	131.84	2.11	13.10	232.51

As TiO$_2$ in complex with GO becomes a TiO$_2$/GO composite, a significant enhancement in the specific surface area was observed, which is in agreement with the reported value of the specific surface area of the composite.[49] Formation of TiO$_2$/GO reduced particle agglomeration due to both TiO$_2$ and GO, yielding a BET surface area of 145.77 m^2/g and a pore diameter of 6.18 nm. In the case of precious metal−TiO$_2$/GO composites, Ag−TiO$_2$/GO, Pd−TiO$_2$/GO, and Cu−TiO$_2$/GO exhibited BET surface areas of 100.36, 214.51, and 131.84 m^2/g, respectively. Pore sizes of Ag−TiO$_2$/GO, Pd−TiO$_2$/GO, and Cu−TiO$_2$/GO were 4.76, 3.28, and 2.43 nm, respectively.

Photoreduction of CO$_2$. Photocatalytic performance of the composites was tested in the photoreduction of CO$_2$ to ethanol. Each of the Ag−TiO$_2$/GO, Pd−TiO$_2$/GO and Cu−TiO$_2$/GO composites was suspended in a CO$_2$-saturated

aqueous solution in a closed container (Figure S1). The suspension was stirred under a UV lamp for 6 h before the liquid sample was collected for GC analysis. The results from the photoreduction of CO_2 to ethanol were reported as an ethanol production rate (μmol/g_{cat} h) (Figure 8). GO and

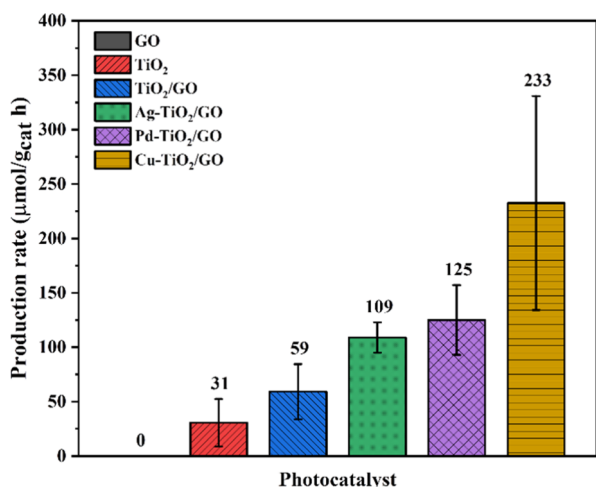**Figure 8.** Ethanol production rate for the GO, TiO_2, TiO_2/GO, Ag–TiO_2/GO, Pd–TiO_2/GO, and Cu–TiO_2/GO photocatalysts.

TiO_2 were tested as control samples, yielding 0 and 31 μmol/g_{cat} h of ethanol, respectively. GO absorbs UV light as well as visible light but provides no photocatalytic ability in reducing CO_2, while TiO_2 catalyzes the reaction and produces ethanol. For the TiO_2/GO composite, the ethanol production rate is 59 μmol/g_{cat} h, which is notably higher than that of the TiO_2 powder. This can be explained as the TiO_2/GO composite

protects TiO_2 from being agglomerated and reduces the pairing rate of electrons and holes in TiO_2. A combination of TiO_2 and GO on the TiO_2/GO composite creates a new type of photocatalyst with superior ability to both TiO_2 and GO. A composite with a precious metal provides an even better photocatalytic performance. Ag–TiO_2/GO, Pd–TiO_2/GO, and Cu–TiO_2/GO yield ethanol production rates of 109 $\pm$ 14, 125 $\pm$ 32, and 232 $\pm$ 98 mol/g_{cat} h, respectively. The precious metals, Ag, Pd, and Cu, can promote the light absorption ability of the composite and provide a transition state for photoelectrons to remain separated from holes.[3]

The Cu–TiO_2/GO composite performs best in our experiment, generating the highest ethanol production rate compared to those of the Ag–TiO_2/GO and Pd–TiO_2/GO. The exceptional performance of Cu–TiO_2/GO combines effects from several factors, such as band gap energy, crystallinity, and the BET surface area (Table 1). The reaction mechanism for the photoreduction of CO_2 to ethanol involves the photocatalytic break down of water molecules and CO_2 dissolution in water (Figure 9). On TiO_2 catalytic sites, water molecules are photocatalytically dissociated into oxygen (O_2), protons (H^+), and electrons (e^-) (eq 1). Electrons can be transferred to TiO_2 and activated from a valence band (VB) to a conductive band (CB) (eq 2), becoming photoelectrons that engage in the photocatalytic reaction. Dissolved CO_2 couples with photoelectrons and becomes an anion carbon dioxide radical (CO_2^-) (eq 3). CO_2^- is the active radical that couples with 12 protons and 10 photoelectrons and yields ethanol (eq 4). The total reaction for the photoreduction of CO_2 (eq 5) can be presented as a combination of dissolved CO_2, 12 protons, and 12 electrons, which generates one molecule of ethanol and three molecules of water. In the case of the Cu–TiO_2/GO composite, copper acts as a transition state for
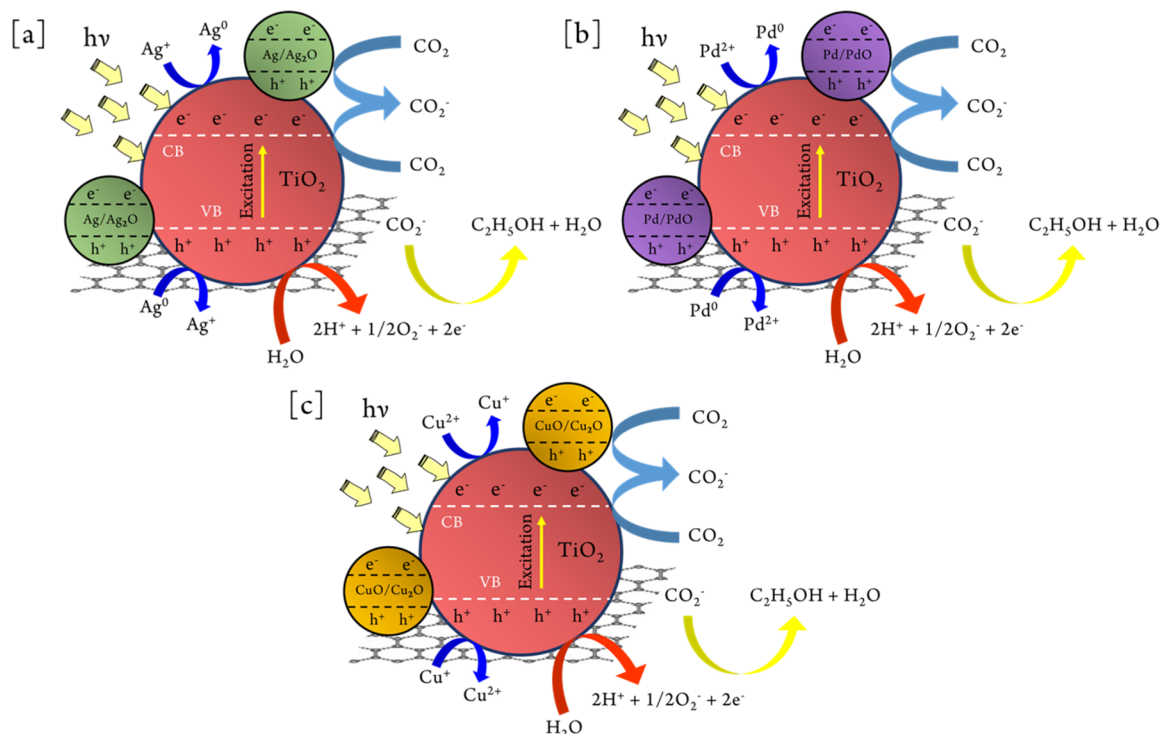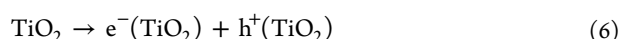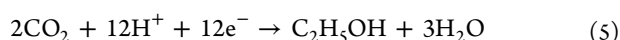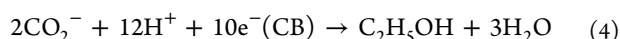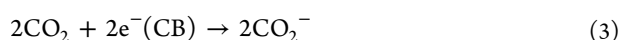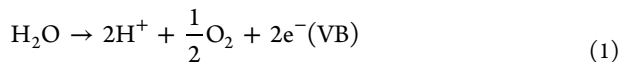

Figure 9. Schematic diagram exhibiting proposed reaction mechanisms for the photoreduction of CO_2 on (a) Ag–TiO_2/GO, (b) Pd–TiO_2/GO, and (c) Cu–TiO_2/GO.

photoelectrons to rest on and separate from photogenerated holes (h^+) (eq 6).[50] The Cu^{2+} radical pairs with photoelectrons from TiO_2 and becomes Cu^+ (eq 7). Cu^+ donates electrons to dissolve CO_2 or CO_2^-, facilitating the photocatalytic reaction and producing more ethanol. The process is reversible because Cu^+ can combine with holes and transform back into Cu^{2+} (eq 8).

$$H_2O \rightarrow 2H^+ + \frac{1}{2}O_2 + 2e^-(VB) \tag{1}$$

$$2e^-(VB) \rightarrow 2e^-(CB) \tag{2}$$

$$2CO_2 + 2e^-(CB) \rightarrow 2CO_2^- \tag{3}$$

$$2CO_2^- + 12H^+ + 10e^-(CB) \rightarrow C_2H_5OH + 3H_2O \tag{4}$$

$$2CO_2 + 12H^+ + 12e^- \rightarrow C_2H_5OH + 3H_2O \tag{5}$$

$$TiO_2 \rightarrow e^-(TiO_2) + h^+(TiO_2) \tag{6}$$

$$Cu^{2+} + e^- \leftrightarrow Cu^+ \tag{7}$$

$$Cu^+ + h^+ \rightarrow Cu^{2+} \tag{8}$$

The role of Ag and Pd as cocatalysts for the TiO_2/GO composite was similar to that of Cu, in which either Ag or Pd can accept electrons and keep them separated from holes. The only difference is the preferred oxidative states, in which Ag switches between the Ag^+ and Ag^0 forms (eqs 9 and 10)[51] and Pd varies between Pd^{2+} and Pd^0 (eqs 11 and 12) (Figure 9).[52]

$$Ag^+ + e^- \leftrightarrow Ag^0 \tag{9}$$

$$Ag + h^+ \rightarrow Ag^+ \tag{10}$$

$$Pd^{2+} + 2e^- \rightarrow Pd^0 \tag{11}$$

$$Pd + 2h^+ \rightarrow Pd^{2+} \tag{12}$$

It is worth mentioning that the liquid C1 products, including methanol and formic acid, were not found in the liquid sample. This could be attributed to the optical properties of the borosilicate glass photoreactor, in which the glass absorbs part of the UVA and UVB and all of the UVC. The phenomenon could affect the energy and density of the photons and photoelectrons, resulting in different reaction rates and pathways.[53] In addition, several reports claimed that graphene in the composite helps stabilize active radicals and intermediates on its carbon structures. This could enhance the probability of two radicals coupling with one another, leading to the formation of ethanol instead of the C1 products.[54,55]

Discussion on the Photocatalytic Performance of the Photocatalysts. GO functions as an excellent substrate for TiO_2 nanoparticles in the TiO_2/GO composite, facilitating the formation of the nanoparticles, immobilizing the nanoparticles and yielding electron−hole separation. GO was also reported as an adsorbent for CO_2 with no significant photocatalytic activity.[56] The graphene content in a $Cu−TiO_2/GO$ composite was investigated using a thermogravimetric analysis technique to be 13.5% of the total mass (Figure S2). For TiO_2, the sample was synthesized following the hydrothermal process without GO and was prone to agglomeration when dried. TiO_2 exhibits a low active BET surface area (9.82 m^2/g) with a wide band gap energy (3.2 eV), which results in a low ethanol production rate (31 $\mu mol/g_{cat}$ h) (Table 1). For TiO_2/GO, the

composite makes use of the GO substrate in immobilizing TiO_2 nanoparticles and transferring electrons. The composite shows great enhancement, as compared to TiO_2, with a higher BET surface area (145.77 m^2/g), a lower band gap energy (3.02 eV), and a larger crystallite size (7.74 nm). These results agree well with an ethanol production rate of 59 $\mu mol/g_{cat}$ h, which is a significant improvement compared to that of TiO_2. For the precious metal-TiO_2/GO composites, a correlation between key parameters and the ethanol production rate becomes complicated. The BET surface area of $Cu−TiO_2/GO$ (131.84 m^2/g) is more than that of $Ag−TiO_2/GO$ (100.36 m^2/g) but less than that of $Pd−TiO_2/GO$ (214.51 m^2/g). The crystallite sizes for $Cu−TiO_2/GO$, $Pd−TiO_2/GO$, and $Ag−TiO_2/GO$ were 13.10, 8.11, and 8.11 nm, revealing that $Cu−TiO_2/GO$ contains a bigger grain size in the polycrystal structure compared to the other composites. The band gap energies for $Cu−TiO_2/GO$, $Pd−TiO_2/GO$, and $Ag−TiO_2/GO$ were 2.11, 3.09, and 2.92 eV, showing that $Cu−TiO_2/GO$ requires less energy to generate photoelectrons. We believe that the key parameters, the BET surface area, band gap energy, and crystallite size, combinedly contributes to the photocatalytic ability of the photocatalyst. There is also possibility for other gas products to generate but not analyzed in our system. The Cu-doped photocatalyst, which promotes CO_2 adsorption and generation of the C2 product then becomes more appealing.[8] In our research work, the ethanol production rate is considered the main goal. Therefore, the $Cu−TiO_2/GO$ composite was chosen here for further studies.

Photocatalytic Performance of the $Cu−TiO_2/GO$ Composite with Different Cu Loadings. The $Cu−TiO_2/GO$ composites were synthesized following the hydrothermal reaction. In the previous tests, 0.71 mL titanium butoxide (0.1 g Ti) was mixed with 3.8 g copper nitrate (0.001 g Cu), creating a 1/100 (w/w) Cu/Ti ratio for the composite (1% $Cu−TiO_2/GO$). Different concentrations of copper nitrate were used during the synthesis to generate 0.5% $Cu−TiO_2/GO$ and 2% $Cu−TiO_2/GO$ composites. The percent of the metal loading on the composites was determined via XRF to be 0.497, 1.090, and 2.031% for the 0.5, 1, and 2% $Cu−TiO_2/GO$ composites, respectively (Table S1). Photocatalytic performance of the composites was compared in the photoreduction of CO_2. 0.5% $Cu−TiO_2/GO$, 1% $Cu−TiO_2/GO$, and 2% $Cu−TiO_2/GO$ exhibit ethanol production rates of 27 ± 5, 233 ± 98, and 30 ± 6 $\mu mol/g_{cat}$ h, respectively (Figure 10). Band gap energies for 0.5% $Cu−TiO_2/GO$, 1% $Cu−TiO_2/GO$, and 2% $Cu−TiO_2/GO$ [Figure 10 (INSET)] were determined to be 3.10, 2.11, and 2.85 eV, respectively. Although it was not clear which parameters contribute most to the photocatalytic performance of the composite, we believe that the optical band gap was the key to the performance of the materials. Variations in the Cu loading could significantly affect the physical structure, optical properties, and the amount of active area of the composite. This part is under investigation in our research group, hoping to elucidate the effects of copper loadings on the composite.

■ **CONCLUSIONS**

In this research, precious metal−TiO_2/GO composites were synthesized via a hydrothermal process and utilized in the photoreduction of CO_2 to ethanol. The $Ag−TiO_2/GO$, $Pd−TiO_2/GO$, and $Cu−TiO_2/GO$ composites exhibit ethanol production rates of 109, 125, and 233 $\mu mol/g_{cat}$ h, outperforming TiO_2/GO (59 $\mu mol/g_{cat}$ h), TiO_2 (31 $\mu mol/g_{cat}$
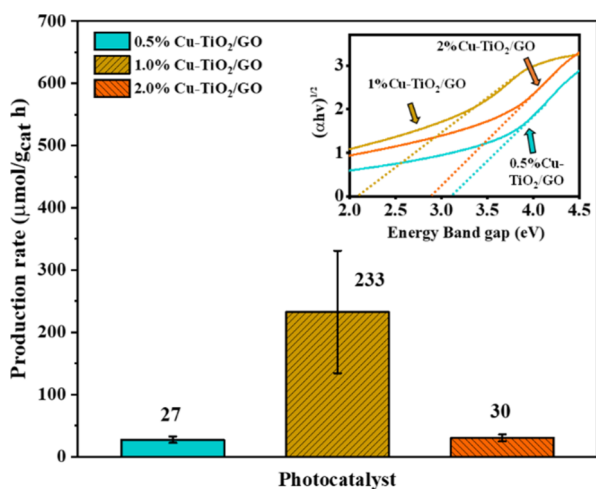
Figure 10. Ethanol production rates for 0.5% Cu−TiO$_2$/GO, 1% Cu−TiO$_2$/GO, and 2% Cu−TiO$_2$/GO.

h), and GO (0 μmol/g$_{cat}$ h). Cu−TiO$_2$/GO showed the best photocatalytic performance, which could be attributed to remarkable key parameters, including a high BET surface area, a narrowed band gap energy, and a big crystallite size. One issue regarding the Cu−TiO$_2$/GO composite is sensitivity to the amount of Cu loading because a slight difference in the loading causes a drastic change in photocatalytic performance. Photoreduction of CO$_2$ to ethanol is one important approach that deals with CO$_2$ emissions and produces liquid energy. Finding an effective catalyst is one of the keys to advancement of the technology.

■ EXPERIMENTAL SECTION

Synthesis of Graphene Oxide. GO powder was synthesized relying on a path of chemical exfoliation. Briefly, 2 g graphite flakes (Alfa Aesar, 99.9%, 10 mesh) were mixed with 1 g sodium nitrate (NaNO$_3$, Fluka Chemika, 99%) and 50 mL sulfuric acid (concentrated H$_2$SO$_4$, ACl Labscan, 98%) in a 250 mL flask. The mixture was stirred continuously in an ice bath (∼0 °C) for 2 h while 7.3 g potassium permanganate (KMnO$_4$, UNIVAR, 99.0%) was slowly added. The mixture was removed from the bath and stirred for another 2.5 h at room temperature (∼30 °C). The graphite flakes were intercalated using potassium permanganate, oxidized, delaminated, and suspended in the mixture. The mixture became viscous and was diluted with 90 mL DI water. A solution of 7 mL hydrogen peroxide (H$_2$O$_2$, Mercks, 30%) and 55 mL DI water was then added to the mixture to convert excess manganese radicals to manganese oxide (MnO$_2$). MnO$_2$ is soluble in an acid solution and can be filtered out along with the filtrate using vacuum filtration and a micro filter paper (GF/C, Whatman). GO was obtained as a brownish powder and rinsed sequentially with 3% v/v hydrochloric acid (HCl, ACl Labscan, 37%) and DI water. The powder was then dried in an oven at 60 °C for 24 h and kept in a desiccator for future use.

One-Step Hydrothermal Synthesis of Precious Metal−TiO$_2$/GO Composites. The one-step synthesis utilizes a hydrothermal process that yields good control over crystal growth and consistent quality of the TiO$_2$ and composites. The reaction occurs inside a teflon-lined autoclave hydrothermal reactor, where GO along with a precious metal precursor and a titanium precursor are mixed and thermally

treated. The mass ratio of precursors (Ag/Ti, Pd/Ti, and Cu/Ti) was controlled at 1/100 (w/w), achieving 1% Ag−TiO$_2$/GO, 1% Pd−TiO$_2$/GO, and 1% Cu−TiO$_2$/GO composites. The amount of precious metal loading on the composite was quantified using the XRF (Table S1) to be 0.906, 0.776, and 1.090% for 1% Ag−TiO$_2$/GO, 1% Pd−TiO$_2$/GO, and 1% Cu−TiO$_2$/GO, respectively.

Synthesis of the Ag−TiO$_2$/GO Composite. 0.71 mL titanium (IV) butoxide (C$_{16}$H$_{36}$O$_4$Ti, Sigma-Aldrich) was dissolved in 20 mL ethanol and mixed with 10 mL DI water. The mixture was vigorously stirred while 1.57 mg silver nitrate (AgNO$_3$, Poch), 2.73 mg trisodium citrate (Na$_3$C$_6$H$_5$O$_7$· 2H$_2$O, Ajax Finechem), and 0.35 mg sodium borohydride (NaBH$_4$, Sigma-Aldrich) were added. The GO suspension was prepared by sonicating 15 mg GO in 10 mL DI water. The suspension was slowly added to the mixture for a 10 min period. Then, the mixture was transferred to a hydrothermal reactor and heated at 180 °C for 7 h. The composite powder was obtained via vacuum filtration and dried at 105 °C for 3 h.

Synthesis of the Pd−TiO$_2$/GO Composite. A solution of 0.71 mL titanium (IV) butoxide in 20 mL ethanol was mixed with 10 mL DI water and stirred. The 1.67 mg palladium (II) chloride (PdCl$_2$, Sigma-Aldrich) precursor was added to the solution along with 2.76 mg trisodium citrate and 0.36 mg of sodium borohydride. The GO suspension (1.5 mg GO/mL) was added to the mixture. The mixture was then transferred to a hydrothermal reactor and heated at 180 °C for 7 h. The solid powder was obtained and dried at 105 °C for 3 h.

Synthesis of the Cu−TiO$_2$/GO Composite. The titanate solution was prepared by mixing 0.71 mL titanium (IV) butoxide with 20 mL ethanol and 10 mL DI water. The 3.8 mg copper (II) nitrate (Cu(NO$_3$)$_2$·3H$_2$O, Sigma-Aldrich) precursor was added to the titanate solution. The mixture was adjusted to pH 12 using 1 M sodium hydroxide solution, followed by the addition of 1.79 mg sodium borohydride. The mixture was thermally treated in a hydrothermal reactor at 180 °C for 7 h. The composite powder was obtained and dried at 105 °C for 3 h.

Synthesis of the TiO$_2$/GO Composite. The TiO$_2$/GO composite was synthesized and used as a control sample. 0.71 mL titanium butoxide was mixed with 20 mL ethanol and 10 mL DI water. A solution of 15 mg GO in 10 mL DI water was slowly added to the mixture, which was then transferred to a hydrothermal reactor and heated at 180 °C for 7 h. The TiO$_2$/GO powder was filtered from the solution, dried at 105 °C for 3 h, and kept in a desiccator for future use.

Sample Characterizations. Graphene and composite materials were characterized for their physical, crystallographic, and chemical properties using various analytical instruments. Physical geometry was analyzed using a field-emission scanning electron microscope (Hitachi SU8010) and a transmission electron microscope (Hitachi H-7650). Crystallography was analyzed using an X-ray diffractometer (Miniflex II, Copper K α radiation, λ = 1.54 A). Chemical functionalities were investigated by a Fourier transform infrared spectrometer (FT/IR-6800, Jasco). The chemical component and element analysis was carried out via an X-ray photoelectron spectrometer (Kratos Model Axis Ultra DLD) and X-ray fluorescence spectrometer (Bruker S8 Tiger). A simultaneous TGA (NETZSCH STA 449 F5 Jupiter) technique was employed to verify the graphene content of the photocatalyst. The samples were heated in an alumina crucible at a heating rate of 20 °C/min from room temperature to 1000 °C in a

nitrogen environment. Optical properties were analyzed by UV−visible spectroscopy (UV−vis; 1800 Shimadzu). The BET surface area and pore sizes of the catalyst were studied using an autosorb surface analyzer (Quanta-chrome). The BET model was applied for determining the monolayer coverage area while the BJH model was adopted for the calculation of the pore size distribution. Relative pressures (equilibrium pressure/saturation pressure of nitrogen, p/p_0) were varied in a window of 0.02 to 1.

From the UV−vis spectra, optical band gap energy can be determined using the Tauc correlation (eq 13)

$$(\alpha h\nu)^{1/n} = \alpha_0(h\nu - E_g) \tag{13}$$

where α is the absorption coefficient $(1/dA)$, d is the thickness of the cuvette cell (1 cm), A is the light absorbance value, $h\nu$ is the photon energy (eV), E_g is the optical band gap energy (eV), α_0 is the constant band tailing parameter, and n is the power factor ($n = 2$ for an indirect transition mode).

From the XRD spectra, the crystallite size of the sample was determined from the major peak using the Debye−Scherrer equation (eq 14)

$$D = 0.9\lambda/\beta \cos\theta \tag{14}$$

where λ is the wavelength of the X-ray beam (0.1540 nm), β is the fwhm of the XRD peak, θ is the diffraction angle, and D is the crystallite size.

Photocatalytic Conversion of CO_2 to Ethanol. The photoreduction of CO_2 took place in a closed chamber under UV radiation (Philips, 160 W: Mercury lamp) (Figure S1). Composite powder of 0.1 mg/mL was suspended in DI water and held in a 25 mL borosilicate container (DURAN). CO_2 gas was bubbled through the suspension for 20 min at a flow rate of 0.1 L/min, creating dissolved CO_2 for the following photoreduction. The pH value of the suspension before and after CO_2 purging was ∼5 and ∼4, respectively. The reaction lasted for 6 h, followed by a collection of liquid samples. The samples were obtained by filtrating the suspension with a syringe filter (FILTREX, Nylon Syringe Filter, 0.2 μm, 13 mm), and were analyzed for ethanol composition. The composition analysis was performed using gas chromatography (GC PerkinElmer Clarus 680), following the EPA method 308 with a flame ionization detector and a DB WAX column (Agilent Technologies) (Figures S4 and S5). The column was preheated at 45 °C for 3 min, raised to 70 °C for 2.5 min, and held steady at 200 °C, while the injector temperature and detector temperature were set at 250 °C.

■ ASSOCIATED CONTENT

⑤ Supporting Information

The Supporting Information is available free of charge at https://pubs.acs.org/doi/10.1021/acsomega.1c05799.

> 25 mL photoreactor positioned in the chamber, under a UV lamp; thermogravimetric analysis of Cu−TiO_2/GO; amount of element loading in Ag−TiO_2/GO, Pd−TiO_2/GO, and Cu−TiO_2/GO composites as analyzed by XRF; EDS and SEM images of the Cu−TiO_2/GO composite; GC curve showing a peak of ethanol; and calibration plot for the GC analysis of ethanol (PDF)

■ AUTHOR INFORMATION

Corresponding Author

Sira Srinives − *Nanocomposite Engineering Laboratory (NanoCEN), Department of Chemical Engineering, Faculty of Engineering, Mahidol University, Salaya, Nakornpathom 73170, Thailand;* ⓞ orcid.org/0000-0002-7890-1103; Email: sira.sri@mahidol.edu

Authors

Napat Lertthanaphol − *Nanocomposite Engineering Laboratory (NanoCEN), Department of Chemical Engineering, Faculty of Engineering, Mahidol University, Salaya, Nakornpathom 73170, Thailand*

Natpichan Pienutsa − *Nanocomposite Engineering Laboratory (NanoCEN), Department of Chemical Engineering, Faculty of Engineering, Mahidol University, Salaya, Nakornpathom 73170, Thailand*

Kittapas Chusri − *Nanocomposite Engineering Laboratory (NanoCEN), Department of Chemical Engineering, Faculty of Engineering, Mahidol University, Salaya, Nakornpathom 73170, Thailand*

Thirawit Sornsuchat − *Nanocomposite Engineering Laboratory (NanoCEN), Department of Chemical Engineering, Faculty of Engineering, Mahidol University, Salaya, Nakornpathom 73170, Thailand*

Prowpatchara Chanthara − *Nanocomposite Engineering Laboratory (NanoCEN), Department of Chemical Engineering, Faculty of Engineering, Mahidol University, Salaya, Nakornpathom 73170, Thailand*

Panpailin Seeharaj − *Advanced Materials Research Unit, Department of Chemistry, Faculty of Science, King Mongkut's Institute of Technology Ladkrabang, Bangkok 10520, Thailand;* ⓞ orcid.org/0000-0003-3200-2601

Pattaraporn Kim-Lohsoontorn − *Center of Excellence on Catalysis and Catalytic Reaction Engineering, Department of Chemical Engineering, Faculty of Engineering, Chulalongkorn University, Bangkok 10330, Thailand*

Complete contact information is available at:
https://pubs.acs.org/10.1021/acsomega.1c05799

Notes

The authors declare no competing financial interest.

■ REFERENCES

(1) Pilorgé, H.; McQueen, N.; Maynard, D.; Psarras, P.; He, J.; Rufael, T.; Wilcox, J. Cost Analysis of Carbon Capture and Sequestration of Process Emissions from the U.S. Industrial Sector. *Environ. Sci. Technol.* **2020**, *54*, 7524−7532.

(2) Almomani, F.; Bhosale, R.; Khraisheh, M.; Kumar, A.; Tawalbeh, M. Photocatalytic conversion of CO_2 and H_2O to useful fuels by nanostructured composite catalysis. *Appl. Surf. Sci.* **2019**, *483*, 363−372.

(3) Seeharaj, P.; Kongmun, P.; Paiplod, P.; Prakobmit, S.; Sriwong, C.; Kim-Lohsoontorn, P.; Vittayakorn, N. Ultrasonically-assisted surface modified $TiO_2/rGO/CeO_2$ heterojunction photocatalysts for conversion of CO_2 to methanol and ethanol. *Ultrason. Sonochem.* **2019**, *58*, 104657.

(4) Xi, G.; Ouyang, S.; Ye, J. General synthesis of hybrid TiO_2 mesoporous "french fries" toward improved photocatalytic conversion of CO_2 into hydrocarbon fuel: a case of TiO_2/ZnO. *Chemistry* **2011**, *17*, 9057−9061.

(5) Yang, L.; Yu, L. E.; Ray, M. B. Degradation of paracetamol in aqueous solutions by TiO_2 photocatalysis. *Water Res.* **2008**, *42*, 3480−3488.

(6) Wang, S.; Pan, L.; Song, J.-J.; Mi, W.; Zou, J.-J.; Wang, L.; Zhang, X. Titanium-defected undoped anatase TiO_2 with p-type conductivity, room temperature ferromagnetism and remarkable photocatalytic performance. *J. Am. Chem. Soc.* **2015**, *137*, 2975−2983.

(7) Lin, Y.; Ferronato, C.; Deng, N.; Chovelon, J.-M. Study of benzylparaben photocatalytic degradation by TiO_2. *Appl. Catal., B* **2011**, *104*, 353−360.

(8) Ali, S.; Razzaq, A.; Kim, H.; In, S.-I. Activity, selectivity, and stability of earth-abundant $CuO/Cu_2O/Cu^0$-based photocatalysts toward CO_2 reduction. *Chem. Eng. J.* **2022**, *429*, 131579.

(9) Vasilaki, E.; Georgaki, I.; Vernardou, D.; Vamvakaki, M.; Katsarakis, N. Ag-loaded TiO_2/reduced graphene oxide nanocomposites for enhanced visible-light photocatalytic activity. *Appl. Surf. Sci.* **2015**, *353*, 865−872.

(10) Khan, S. A.; Arshad, Z.; Shahid, S.; Arshad, I.; Rizwan, K.; Sher, M.; Fatima, U. Synthesis of TiO_2/Graphene oxide nanocomposites for their enhanced photocatalytic activity against methylene blue dye and ciprofloxacin. *Composites, Part B* **2019**, *175*, 107120.

(11) Pienutsa, N.; Roongruangsree, P.; Seedokbuab, V.; Yannawibut, K.; Phatoomvijitwong, C.; Srinives, S. SnO_2-graphene composite gas sensor for a room temperature detection of ethanol. *Nanotechnology* **2021**, *32*, 115502.

(12) Williams, G.; Seger, B.; Kamat, P. V. TiO_2-Graphene Nanocomposites. UV-Assisted Photocatalytic Reduction of Graphene Oxide. *ACS Nano* **2008**, *2*, 1487−1491.

(13) Tang, B.; Dai, Y.; Sun, Y.; Chen, H.; Wang, Z. Graphene and MOFs co-modified composites for high adsorption capacity and photocatalytic performance to remove pollutant under both UV- and visible-light irradiation. *J. Solid State Chem.* **2020**, *284*, 121215.

(14) Yang, H. A short review on heterojunction photocatalysts: Carrier transfer behavior and photocatalytic mechanisms. *Mater. Res. Bull.* **2021**, *142*, 111406.

(15) Ali, S.; Razzaq, A.; In, S.-I. Development of graphene based photocatalysts for CO_2 reduction to C1 chemicals: A brief overview. *Catal. Today* **2019**, *335*, 39−54.

(16) Wang, H.; Zhang, L.; Chen, Z.; Hu, J.; Li, S.; Wang, Z.; Liu, J.; Wang, X. Semiconductor heterojunction photocatalysts: design, construction, and photocatalytic performances. *Chem. Soc. Rev.* **2014**, *43*, 5234−5244.

(17) Saleem, H.; Habib, A. Study of band gap reduction of TiO_2 thin films with variation in GO contents and use of TiO_2/Graphene composite in hybrid solar cell. *J. Alloys Compd.* **2016**, *679*, 177−183.

(18) Zou, F.; Hu, J.; Miao, W.; Shen, Y.; Ding, J.; Jing, X. Synthesis and Characterization of Enhanced Photocatalytic Activity with Li +-Doping Nanosized TiO_2 Catalyst. *ACS Omega* **2020**, *5*, 28510−28516.

(19) Zhang, Z.; Yang, W.; Zou, X.; Xu, F.; Wang, X.; Zhang, B.; Tang, J. One-pot, solvothermal synthesis of TiO_2-graphene composite nanosheets. *J. Colloid Interface Sci.* **2012**, *386*, 198−204.

(20) Yadav, H. M.; Kim, J.-S. Solvothermal synthesis of anatase TiO_2-graphene oxide nanocomposites and their photocatalytic performance. *J. Alloys Compd.* **2016**, *688*, 123−129.

(21) Li, G.; Huang, J.; Chen, J.; Deng, Z.; Huang, Q.; Liu, Z.; Guo, W.; Cao, R. Highly Active Photocatalyst of Cu_2O/TiO_2 Octahedron for Hydrogen Generation. *ACS Omega* **2019**, *4*, 3392−3397.

(22) Fan, Y.; Lu, H.-T.; Liu, J.-H.; Yang, C.-P.; Jing, Q.-S.; Zhang, Y.-X.; Yang, X.-K.; Huang, K.-J. Hydrothermal preparation and electrochemical sensing properties of TiO_2-graphene nanocomposite. *Colloids Surf., B* **2011**, *83*, 78−82.

(23) Najafi, M.; Kermanpur, A.; Rahimipour, M. R.; Najafizadeh, A. Effect of TiO_2 morphology on structure of TiO_2-graphene oxide nanocomposite synthesized via a one-step hydrothermal method. *J. Alloys Compd.* **2017**, *722*, 272−277.

(24) Zhang, D.; Pu, X.; Ding, G.; Shao, X.; Gao, Y.; Liu, J.; Gao, M.; Li, Y. Two-phase hydrothermal synthesis of TiO_2−graphene hybrids with improved photocatalytic activity. *J. Alloys Compd.* **2013**, *572*, 199−204.

(25) Li, W.; Liang, R.; Zhou, N. Y.; Pan, Z. Carbon Black-Doped Anatase TiO_2 Nanorods for Solar Light-Induced Photocatalytic Degradation of Methylene Blue. *ACS Omega* **2020**, *5*, 10042−10051.

(26) Nagaraju, P.; Alsalme, A.; Alswieleh, A.; Jayavel, R. Facile in-situ microwave irradiation synthesis of TiO_2/graphene nanocomposite for high-performance supercapacitor applications. *J. Electroanal. Chem.* **2018**, *808*, 90−100.

(27) Yang, Y.; Xu, L.; Wang, H.; Wang, W.; Zhang, L. TiO_2/graphene porous composite and its photocatalytic degradation of methylene blue. *Mater. Des.* **2016**, *108*, 632−639.

(28) Khalid, N. R.; Ahmed, E.; Hong, Z.; Ahmad, M.; Zhang, Y.; Khalid, S. Cu-doped TiO_2 nanoparticles/graphene composites for efficient visible-light photocatalysis. *Ceram. Int.* **2013**, *39*, 7107−7113.

(29) Ren, Y.; Sun, C.; Li, K.; Wang, L.; Song, M. Preparation of TiO_2−reduced graphene oxide−Pd nanocomposites for phenol photocatalytic degradation. *Ceram. Int.* **2016**, *42*, 1339−1344.

(30) Zhang, J.; Yang, H.; Shen, G.; Cheng, P.; Zhang, J.; Guo, S. Reduction of graphene oxide via L-ascorbic acid. *Chem. Commun.* **2010**, *46*, 1112−1114.

(31) Ahmed, A. S.; Ahamad, T.; Ahmad, N.; Khan, M. Z. Removal enhancement of acid navy blue dye by GO-TiO_2 nanocomposites synthesized using sonication method. *Mater. Chem. Phys.* **2019**, *238*, 121906.

(32) Ghorbani, M.; Abdizadeh, H.; Golobostanfard, M. R. Reduction of Graphene Oxide via Modified Hydrothermal Method. *Procedia Mater. Sci.* **2015**, *11*, 326−330.

(33) Aguilar, T.; Navas, J.; Alcántara, R.; Fernández-Lorenzo, C.; Gallardo, J. J.; Blanco, G.; Martín-Calleja, J. A route for the synthesis of Cu-doped TiO_2 nanoparticles with a very low band gap. *Chem. Phys. Lett.* **2013**, *571*, 49−53.

(34) Vijayalakshmi, R.; Rajendran, V. Synthesis and characterization of nano-TiO_2 via different methods. *Arch. Appl. Sci. Res.* **2012**, *4*, 1183−1190.

(35) Yadav, A.; Yadav, M.; Gupta, S.; Popat, Y.; Gangan, A.; Chakraborty, B.; Ramaniah, L. M.; Fernandes, R.; Miotello, A.; Press, M. R.; Patel, N. Effect of graphene oxide loading on TiO_2: Morphological, optical, interfacial charge dynamics-A combined experimental and theoretical study. *Carbon* **2019**, *143*, 51−62.

(36) Yang, M.-Q.; Zhang, N.; Xu, Y.-J. Synthesis of Fullerene-, Carbon Nanotube-, and Graphene-TiO_2 Nanocomposite Photocatalysts for Selective Oxidation: A Comparative Study. *ACS Appl. Mater. Interfaces* **2013**, *5*, 1156−1164.

(37) Bokhimi, X.; Morales, A.; Novaro, O.; López, T.; Chimal, O.; Asomoza, M.; Gómez, R. Effect of Copper Precursor on the Stabilization of Titania Phases, and the Optical Properties of Cu/TiO_2 Prepared with the Sol-Gel Technique. *Chem. Mater.* **1997**, *9*, 2616−2620.

(38) Zhang, J.; Zhou, P.; Liu, J.; Yu, J. New understanding of the difference of photocatalytic activity among anatase, rutile and brookite TiO_2. *Phys. Chem. Chem. Phys.* **2014**, *16*, 20382−20386.

(39) Xu, H.; Ouyang, S.; Li, P.; Kako, T.; Ye, J. High-active anatase TiO_2 nanosheets exposed with 95% {100} facets toward efficient H_2 evolution and CO_2 photoreduction. *ACS Appl. Mater. Interfaces* **2013**, *5*, 1348−1354.

(40) Lewin, E.; Persson, P. O. Å.; Lattemann, M.; Stüber, M.; Gorgoi, M.; Sandell, A.; Ziebert, C.; Schäfers, F.; Braun, W.; Halbritter, J.; Ulrich, S.; Eberhardt, W.; Hultman, L.; Siegbahn, H.; Svensson, S.; Jansson, U. On the origin of a third spectral component of C1s XPS-spectra for nc-TiC/a-C nanocomposite thin films. *Surf. Coat. Technol.* **2008**, *202*, 3563−3570.

(41) Luo, L.; Yang, Y.; Zhang, A.; Wang, M.; Liu, Y.; Bian, L.; Jiang, F.; Pan, X. Hydrothermal synthesis of fluorinated anatase TiO_2/ reduced graphene oxide nanocomposites and their photocatalytic degradation of bisphenol A. *Appl. Surf. Sci.* **2015**, *353*, 469−479.

(42) Akhavan, O.; Ghaderi, E. Photocatalytic Reduction of Graphene Oxide Nanosheets on TiO_2 Thin Film for Photo-inactivation of Bacteria in Solar Light Irradiation. *J. Phys. Chem. C* **2009**, *113*, 20214−20220.

(43) Wang, T.; Tang, T.; Gao, Y.; Chen, Q.; Zhang, Z.; Bian, H. Hydrothermal preparation of Ag-TiO_2-reduced graphene oxide ternary microspheres structure composite for enhancing photo-catalytic activity. *Phys. E* **2019**, *112*, 128−136.

(44) Wang, T.; Wei, J.; Shi, H.; Zhou, M.; Zhang, Y.; Chen, Q.; Zhang, Z. Preparation of electrospun Ag/TiO_2 nanotubes with enhanced photocatalytic activity based on water/oil phase separation. *Phys. E* **2017**, *86*, 103−110.

(45) Zhang, B.; Yang, F.; Zhang, X.; Wu, N.; Liu, B.; Li, Y. Construction of Graphene-Wrapped Pd/TiO_2 Hollow Spheres with Enhanced Anti-CO Poisoning Capability toward Photoassisted Methanol Oxidation Reaction. *ACS Sustainable Chem. Eng.* **2021**, *9*, 1352−1360.

(46) Iatsunskyi, I.; Gottardi, G.; Micheli, V.; Canteri, R.; Coy, E.; Bechelany, M. Atomic layer deposition of palladium coated TiO_2/Si nanopillars: ToF-SIMS, AES and XPS characterization study. *Appl. Surf. Sci.* **2021**, *542*, 148603.

(47) Zhang, H.; Guo, L.-H.; Wang, D.; Zhao, L.; Wan, B. Light-induced efficient molecular oxygen activation on a Cu(II)-grafted TiO_2/graphene photocatalyst for phenol degradation. *ACS Appl. Mater. Interfaces* **2015**, *7*, 1816−1823.

(48) Chen, H. Y.; Chen, L.; Lin, J.; Tan, K. L.; Li, J. Copper Sites in Copper-Exchanged ZSM-5 for CO Activation and Methanol Synthesis:XPS and FTIR Studies. *Inorg. Chem.* **1997**, *36*, 1417−1423.

(49) Štengl, V.; Popelková, D.; Vláčil, P. TiO_2−Graphene Nano-composite as High Performance Photocatalysts. *J. Phys. Chem. C* **2011**, *115*, 25209−25218.

(50) Liu, L.; Zhao, C.; Miller, J. T.; Li, Y. Mechanistic Study of CO_2 Photoreduction with H_2O on Cu/TiO_2 Nanocomposites by in Situ X-ray Absorption and Infrared Spectroscopies. *J. Phys. Chem. C* **2016**, *121*, 490−499.

(51) Tahir, M. Well-designed $ZnFe_2O_4$/Ag/TiO_2 nanorods heterojunction with Ag as electron mediator for photocatalytic CO_2 reduction to fuels under UV/visible light. *J. CO_2 Util.* **2020**, *37*, 134−146.

(52) Sakai, Y.; Shimanaka, A.; Shioi, M.; Kato, S.; Satokawa, S.; Kojima, T.; Yamasaki, A. Fabrication of high-sensitivity palladium loaded tungsten trioxide photocatalyst by photodeposite method. *Catal. Today* **2015**, *241*, 2−7.

(53) Fu, J.; Jiang, K.; Qiu, X.; Yu, J.; Liu, M. Product selectivity of photocatalytic CO_2 reduction reactions. *Mater. Today* **2020**, *32*, 222−243.

(54) Tu, W.; Zhou, Y.; Liu, Q.; Yan, S.; Bao, S.; Wang, X.; Xiao, M.; Zou, Z. An In Situ Simultaneous Reduction-Hydrolysis Technique for Fabrication of TiO_2-Graphene 2D Sandwich-Like Hybrid Nano-sheets: Graphene-Promoted Selectivity of Photocatalytic-Driven Hydrogenation and Coupling of CO_2 into Methane and Ethane. *Adv. Funct. Mater.* **2013**, *23*, 1743−1749.

(55) Sorcar, S.; Thompson, J.; Hwang, Y.; Park, Y. H.; Majima, T.; Grimes, C. A.; Durrant, J. R.; In, S. High-rate solar-light photo-conversion of CO_2 to fuel: controllable transformation from C_1 to C_2 products. *Energy Environ. Sci.* **2018**, *11*, 3183−3193.

(56) Shrivastava, S.; Thomas, S.; Sobhan, C. B.; Peterson, G. P. An experimental investigation of the CO_2 adsorption performance of graphene oxide forms. *Int. J. Refrig.* **2018**, *96*, 179−190.